Study of CO_2 Laser-induced Thermal Stress Mechanisms on Decorative Soda-lime Glass

Alex Capelle[1,2], Barthélemy Aspe[1], Olga Shavdina[2], Babacar Diallo[3], Nadia Pellerin[3], Martin Depardieu[2], Anne-Lise Thomann[1], and Nadjib Semmar[*1]

[1] *GREMI – Université d'Orléans CNRS UMR 7344, 14 Rue d'Issoudun, 45067 Orléans, France*
[2] *Décor World Services (DWS), 1 Av. du Champ de Mars, 45100 Orléans, France*
[3]*CEMHTI - CNRS UPR 3079, 1 Av. de la Recherche Scientifique, 45100 Orléans, France*
[*]*Corresponding author's e-mail:nadjib.semmar@univ-orleans.fr*

In this study, we examine texturing features on soda-lime (SDL) silicate glass bottles achieved using a Carbon Dioxide (CO_2) laser with continuous wave power (25 W at 10.6 µm). SDL glass samples were subjected to irradiation in both static and dynamic modes. In the static mode, exposure time (τ_{ON}) varied from 10 µs to 2 ms, while the dynamic mode involved scan velocities (line) ranging from 20 mm/s to 3 m/s. Our evaluation focused on engraving rate, fracture morphologies, and damaged zone characteristics. Using optical microscopy and stylus profilometry, we identified three distinct process regimes: partial texturing, full texturing, and material removal. To gain insights into the underlying mechanisms of the process, we developed a 2D axisymmetric thermo-mechanical model using COMSOL Multiphysics®. This model allowed us to compute the transient laser-induced thermal stress and the relaxation occurring in the viscoelastic state of SDL. Remarkably, our simulation demonstrated a correlation between the tensile cracking threshold of SDL (0.1 GPa) and experimental data. By comapring the experimental and simulation results, we were able to estimate the damaged zone diameter with an accuracy of ±3% in the partial texturing regime and an overall accuracy of ±8% across all regimes in the static mode.

DOI: 10.2961/jlmn.2023.03.2009
Keywords: glass marking, CO_2 laser, thermal stress, decoration, crack formation, COMSOL simulation

1. Introduction

Product personalization has represented a growing market since the 2000s in the high value-added consumer products industry *e. g.*, perfumery, wines and spirits, jewelry, and cosmetics [1]. The use of in-store personalization machines allows brands to offer personalization features for a moderate additional cost. When used for a gift, this personalization greatly increases the satisfaction of the recipient and the giver [2]. This feature can also be used by the brands to create event-related limited-edition series *e. g.*, Valentine's Day, directly in the store, avoiding massive destruction of unsold products after the event.

Nowadays, in-store personalization machines rely mainly on CO_2 lasers which are able to mark almost every material used in the packaging industry, *e. g.* wood, plastic, paper, and glass, thanks to their high infrared wavelength. CO_2 lasers are still the most common lasers in the marking industry because of their high efficiency, high power and versatility [3–5].

The main container material for perfumery, wines and spirits is SDL glass [6]. It represents more than 90% of the worldwide production of glass [7]. This common glass is known for its high absorption coefficient ($>10^3$ cm^{-1}) in the infrared (IR) spectral region 9 to 13 µm [8–10] leading to a high temperature rise of the irradiated material surface. Additionally, its relatively high coefficient of thermal expansion (9.10^{-6} K^{-1}) creates thermal stress in the material that can sometimes lead to its cracking [11]. Several studies [11–15] have explored methods to improve marking quality by reducing the heat affected zone and therefore removing glass without cracking. Previous work in our lab [16] managed to reduce the cracking effect by studying the heat affected zone for the glass cutting process. Despite these studies, to the best of our knowledge, the thermal-induced fracture initiation and growth in SDL glass has never been studied for fine decoration purposes.

The transient thermal stress experienced by the glass above its transition temperature T_g is a complex phenomenon that induces structural relaxation and material flow. Some models [17,18] that consider these phenomena are based on pure amorphous silica glass for the static condition. Yamamoto *et al.* [15] simulated 3D temperature evolution and estimated thermal stress without considering relaxation phenomena. Based on these previous studies, we chose to simulate the static mode with a COMSOL 2D-axisymmetric plane and use a physical criterion (beam dwell time τ_{dw}) to compare it to the dynamic mode which requires heavier computational resources (3D).

In this article, we will first study the engraving rate, fracture morphologies and damaged zone features from the near-threshold cracking regime to a continuous material ejection regime for both static and dynamic modes. We will discuss the process regime in which process-controllable cracking occurs. The influence of the process parameters for static and dynamic modes is also investigated. Secondly, we will compare experimental data to the simulation using COMSOL Multiphysics that takes structural relaxation into account.

2. Method and materials

2.1 Substrate properties

The chosen substrate is a common commercial small perfume glass bottle of about 10 mL with flat faces measuring 50x30x13 mm outer dimensions (**Fig. 1 (a)**). The inner surface of the bottle is not flat as the samples are formed by blowing and moulding. There is however an area measuring about 30x25 mm with a fairly constant wall thickness of 1.5 mm (**Fig. 1 (b)**). All the engraving tests were performed in this area named engraving area. The sample surface is considered flat because its surface waviness (±200 µm) is small compared to the Rayleigh length of the laser spot (±3.0 mm). Because our sample's material properties are not given by the supplier, we decided to measure its chemical composition by X-fluorescence and compare it with the chemical composition of an SDL glass container from the literature, see **Table 1**. The relation of viscosity to temperature was estimated using Fluegel's material properties simulator [19] based on the measured chemical composition. This preliminary study confirmed the SDL nature of the bottles. All the other SDL material properties were then taken from the literature. The material properties considered for this study and the associated literature references are listed in **Table 2**.

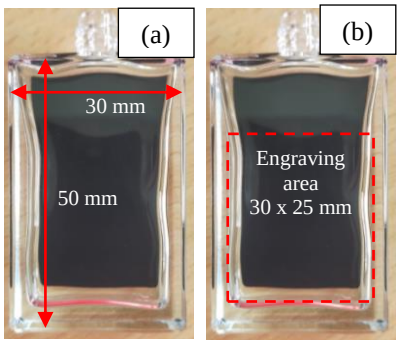

Fig. 1 (a) Photograph of the bottles with their dimensions. **(b)** Engraving area represented with dashed line.

Table 1 Composition of the bottles measured by X-fluorescence.

(%mol)	*Our glass bottles*	*Typical SDL glass* [20]
SiO_2	72	73
CaO	9.9	12
Al_2O_3	2.1	1
Na_2O	15.5	14
K_2O	0.3	
CeO_2	0.1	
Fe_2O_3	0.1	

The temperature dependence of some glass properties has to be taken into account [15,17,21]. When glass is heated to the T_g, the specific heat capacity suddenly increases and remains constant for higher temperatures whereas viscosity drops by several orders of magnitude [22,23]. This drop of viscosity allows any applied stress to relax over time through a characteristic time constant $\tau_{rel}= \eta/G$. The relation of viscosity to temperature is modelled using the empirical Vogel–Fulcher–Tammann (VFT) law **(1)**.

$$\eta(T) = 10^{A_\eta + \frac{B_\eta}{T - C_\eta}} \quad \textbf{(1)}$$

A_η, B_η and C_η are empirical coefficients depending on the material composition, T is the temperature (°C), η the dynamic viscosity (Pa.s) and G the shear modulus (Pa).

The viscoelastic state experienced by the sample at temperatures between T_g and T_m can be represented with mechanical bonds between glass particles [24]. The nature and the configuration of these mechanical bonds can model a viscoelastic behavior. In this case, mechanical bonds are composed of purely Hookian springs and purely viscous damps that relax over time. In this study, we chose to use the standard linear solid (SLS) viscoelasticity model because it only involves the relation of viscosity to the temperature and the shear modulus, and describes both creep recovery and stress relaxation.

2.2 Thermo-mechanical modelling

Following Bäuerle *et al.* [21], depending on the absorption coefficient α of the material and the radius of the laser beam ω_0 hitting its surface, the heat source can be considered as surface heating when the normalized absorption coefficient $\alpha^*=\alpha\omega_0 \gg 10$ and as penetrating when lower. In the case of a CO_2 laser on a SDL glass substrate, the heat source can be considered as a surface heat source because we have a short radiation penetration depth [25] that satisfies the prerequisite assumption $\alpha^*=48 \gg 10$. Moreover, the absorption coefficient has a tendency to increase with temperature, increasing the surface absorption effect [17].

The laser power density involved in this process is on the order of 10^5 W/cm^2 which is not enough to produce non-linear effects but does induce high enough temperature gradients for thermal stress to reach the failure limits of the sample [11].

Following Bennett *et al.* [17], above the stress relaxation temperature the glass can be considered liquid-like. It only supports hydrostatic pressure, converting thermal stress into axial strain. During subsequent cooling, the same relaxation point is encountered but leads to strain freezing which builds up radial tensile stress between the relaxed zone and the unrelaxed surroundings. It is important to note that SDL glass presents a failure stress that is weaker in tensile mode (0.1 GPa with a strain rate of 10 s^{-1}) [26] than in compressive mode (0.8 GPa with a strain rate of 10 s^{-1}) [27].

2.3 FEM Computation

Modelling of the laser-matter interaction was done with the COMSOL Multiphysics® software (release version 6.1). For the laser source, we chose to consider a top-hat beam profile as the laser presents high Transverse Electromagnetic (TEM_{21}) modes in the beam intensity profile. An ablation test on soft material revealed an approximately flat intensity profile.

The steepness of the top-hat profile was set to $0.1\omega_0$ to maintain continuity of the derivatives. The temporal profile was also adapted for continuity with a laser power rise/fall time of 50 µs, which was experimentally measured. The heat transfer in solids and solid mechanics equations were applied to the whole simulated domain using cylindrical coordinate (R, Z, θ).

Table 2 Material properties of our samples and soda-lime silicate glass. *Values are calculated with a properties simulator based on the chemical composition of our samples.

	Material properties		Unit	Ref.
α	Absorption coefficient at 10.6 µm	4800	cm^{-1}	[8, 25, 28]
R	Normal incidence Reflection coefficient	0.16		[11, 15, 25, 28]
K	Thermal conductivity	0.0014*T + 0.8	W/m.K	[17]
C_p	Specific heat	909.8 + 0.3468/T^2 for T<T_g 1430 for T>T_g	J/kg.K	[23]
ρ	Density	2520	kg/m^3	[19, 29]
A_η, B_η, C_η	VFT model coefficient	-3,231, 4800, 357	°C	[19]*
T_g, T_m	Glass transition and melting temperature	672, 1492	°C	[19]*
ΔH_m	Enthalpy of melting	100	kJ/kg	[13]
E	Young's modulus	62	GPa	[11, 15, 29]
G	Bulk Shear Modulus	25.4	GPa	[29]
ν	Poisson's ratio	0.22		[11, 15, 29]
γ	Coefficient of thermal expansion	9	ppm/K	[11, 15, 29]

Thermal expansion is the phenomenon that yields displacements (stress and strain) in the material due to temperature gradients. We will solve the heat diffusion equation **(2)**. The laser heating term **(3)** is set as a boundary condition of the domain **(4)**. The initial state and boundary conditions of the temperature are stated in **(5)**.

$$\rho C_p \frac{\partial T}{\partial t} = \nabla(K\nabla T) \quad \textbf{(2)}$$

$$Q(r,t) = \frac{P(1-R)}{\pi\omega_0^2}\mathcal{H}(\omega_0 - r)\mathcal{H}(t)\mathcal{H}(\tau_{ON} - t) \quad \textbf{(3)}$$

$$\phi(r, z=0, t) = Q(r,t) \quad \textbf{(4)}$$

$$T(r,z,t=0) = T(r,z\to\infty,t) = T(r\to\infty,z,t) = T_0 \quad \textbf{(5)}$$

where Q is the laser heating surface source, P the laser CW power, τ_{ON} the exposure time, H the Heaviside function and T_0=273.15 K the room temperature.

The simulation was run on a 2D-axisymmetric plane of radius r=1 mm and height z=500 µm, divided into 2 subdomains, see **Fig. 2 (a)**. The first one is the interaction region where most of the thermo-mechanical processes occur. This region has a refined free triangular mesh of size 2 µm ±10% and is located at the origin. The dimensions of this subdomain were set to r=2ω_0 and z=2ω_0. The second subdomain is the bulk region with an adaptative coarser free triangular mesh size of 40 µm ±10%, see **Fig. 2 (b)**. These dimensions were chosen to ensure adiabatic conditions and free displacement on the external boundaries of the domain. The simulation time was finely divided into steps of 1 µs from t=0 to t=τ_{ON} to follow the heating of the material which can reach rates of 10^6 K/s. Then, from t=τ_{ON} to t=3τ_{ON}, the time step was lengthened to 10 µs because the material's cooling rate is much slower than its heating. Lastly, we used a logarithmic time step scale from t=3τ_{ON} to t=100τ_{ON} with 10 steps per decade to continue the simulation time until the whole material had cooled to the initial room temperature.

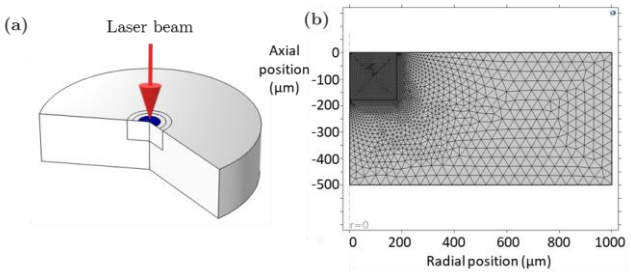

Fig. 2 (a) 3D representation of the simulated domain with irradiated surface coloured. **(b)** Mesh discretization of the domain.

3. Experimental setup

3.1 Engraving system

To engrave SDL glass, we used a 25 W CO_2 laser emitting at 10.6 µm wavelength. On the output of the laser head, **Fig. 3**, there is a galvo-mirror 2D deflection system named scanning head. This scanning head can move the laser beam at velocities ranging from 1 mm/s to 10 m/s in the scanning area of 60*60 mm. The deflected beam is finally focused through a ZnSe flat-field lens with a focal distance 80 mm.

The laser presents high Transverse Electromagnetic Modes, (TEM_{21}) estimated by observation of the ablated profile of a thick PMMA slab. At the focal distance, the laser beam has a radius of ω_0=100±5 µm experimentally measured by a method inspired by Liu *et al.*'s method [30] on anodised aluminium. The diameter is measured along its two main axes. We measured the evolution of the damaged zone on anodised aluminium with increasing energy dose (P/V). This technique allows a precise diameter measurement for a focused beam. The use of anodised aluminium is very convenient for measuring a CO_2 laser beam spot size because only the anodized paint is removed proportionally to the laser fluence, leaving a white mark on a black surface.

The corresponding average irradiance at the working distance is then 80 kW/cm² estimated from the laser beam diameter measurement. The influence of the incident angle is considered negligible. The sample is placed in the scanning area with its surface to be marked at the focal distance of the lens. The marking process is done at atmospheric conditions without gas assistance.

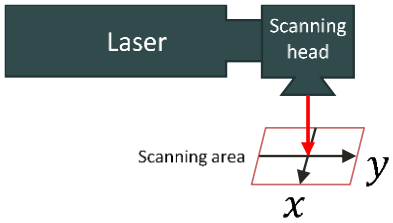

Fig. 3 Scheme of the CO_2 laser engraving system.

3.2 Characterization tools

The markings are characterized with three instruments. The first one is the numerically driven confocal microscope KEYENCE VHX 5000, which can assemble depth profiles using 2D in-plane surface sharpness information to build 3D surfaces. This feature is convenient because it can output large area surface profiles at once. However, measuring transparent media is a difficult task because sharpness information is often retrieved under the surface of the glass and thus creates many artefacts. To overcome this problem, we used a stylus profilometer Bruker DektakXT with a stylus tip diameter of 25 µm and 3 g weight to measure surface profiles of the damaged zone.

A second microscope OLYMPUS SZ61 was used to photograph larger areas.

4. Results

4.1 Crack initiation threshold

The fracture initiation threshold region was studied to estimate the variability of the glass damaging conditions. Five glass bottles were irradiated for different pulse durations, each value being repeated 62 times (2 lines of 31 shots per value of pulse duration). Samples 1, 2 and 3 were independently irradiated and Samples 4.1 and 4.2 were both irradiated at the same time. The comparison between samples irradiated together and independently makes it possible to estimate the variability of the cracking phenomenon and the variability of the laser power between engraving sessions.

We define the engraving rate as the number of damaged sites over the 62 irradiation sites. A site is qualified as "not damaged" when no visible crack is detected at the surface under naked eye observation. Microscope measurements were also done to verify that a naked eye verification was accurate enough to estimate the presence of cracks.

The results in **Fig. 4** show that samples 4.1 and 4.2 present a similar engraving rate. This implies that laser-matter interaction does not depend on the sample and that pulse-to-pulse stability is negligible. However, the differences observed for samples 1, 2, 3 and 4 mean that we have a high variability between consecutive irradiation sessions. Considering the "50% engraving rate" threshold, we see that two independent irradiation sessions can lead to differences of hundredths of microseconds. This difference leads to equivalent power variations between sessions of ±5 W. This value comes from the power compensation to make every measure fit inside the Sample 3 confidence interval. In a nutshell, we have to be careful to always engrave samples in a row in order to compare them.

Finally, we can estimate the "100% engraving rate" threshold as 500 µs. This value is the minimum τ_{ON} process parameter to obtain reliable and repeatable marking.

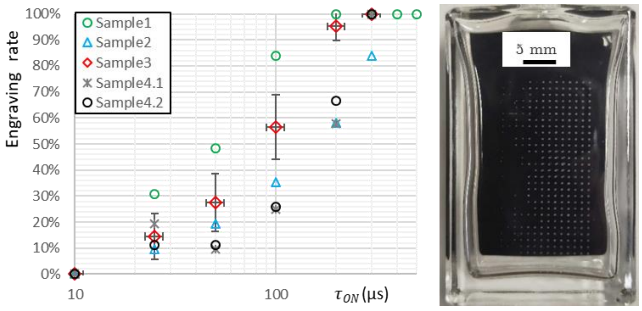

Fig. 4 Engraving rate of 5 different samples irradiated with 8 values of τ_{ON}, each value repeated 62 times. The picture is a photograph of Sample 1. Damaged sites are the small white dots. Vertical error bars are the confidence interval of the 62 attempts and horizontal error bars are the uncertainty based on laser pulse-to-pulse stability (±10%).

4.2 Cracking morphologies of single shot irradiation

The results presented in **Fig. 5** are the damaged zone analysis for the static irradiation condition, named "dot" pattern. They were all made in a row and repeated 6 times because of the random nature of cracking experiments. The micrograph pictures were selected among repeated experiments to illustrate the main features of the cracking morphology. A stylus profilometry measurement systematically accompanies the micrographs to help visualize the 3D nature of the damaged zone. The values of irradiation time τ_{ON} were chosen to encompass the different cracking regimes based on results from **section 4.1**, from a very short exposure of τ_{ON}=10 µs, where no damage is visible, to a constant ablation regime for τ_{ON}>1000 µs. The background colors of **Fig. 5 (b)** and **Fig. 5 (c)** are different because the High Dynamic Range (HDR) option was enabled in the microscope configuration. This option improves color and light intensity rendering but does not influence our measurements.

The dynamic mode, see **Fig. 6,** is done with CW laser irradiation and a moving source relative to the sample at velocity V. The source describes single-pass straight lines in the XY plane on the sample's surface. Velocity values range from 18.8 mm/s to 3000 mm/s. The velocities are converted to dwell-time $\tau_{dw}= 2\omega_0/V$ in order to compare the results of the dynamic mode with the static mode.

4.3 Numerical simulation of the damaged zone

Fig. 7 (a) presents the radial component of the viscoelastic stress tensor σ_{RR} in the RZ plane with the stress relaxation process considered. The other components of the viscoelastic stress tensor were also studied; the results are not shown in the figure but are explained here. The relaxed region in the final state ($t=100\tau_{ON}$) presents a homogeneous compressive stress of $\sigma_{ZZ}\approx0.1$ GPa along the ZZ component. The main shearing stress is found along σ_{RZ} and is in the order of 1 MPa. Other shearing components ($\sigma_{R\theta}$, $\sigma_{Z\theta}$) are equal to 0. Because both compressive and tensile stresses are experienced by the glass during the simulation, we used red for tensile stress and blue for compressive stress. The results are presented for different τ_{ON} and at increasing cooling times proportional to the latter: $t=3\tau_{ON}$ corresponds to significant cooling compared to the maxi-

mum temperature reached during heating and $t=100\tau_{ON}$ corresponds to the time required for the material to return approximately to RT. The radius of the relaxed zone r_r in the final state ($t=100\tau_{ON}$) was compared with the damaged zone radius from experimental data. For the sake of clarity, temperature isovalues in K are shown in black lines on the results pictures. They correspond to T_g, T_m and T_{vap} namely, glass transition temperature, glass melting temperature and silica vaporization temperature. Stress isovalues are also shown on **Fig. 7 (a)**. The first one is 0.1 GPa, the tensile failure stress of SDL glass, and the second value, not visible in our case, is -0.8 GPa, the compressive failure stress of SDL glass. **Fig. 7 (b)** shows the extremum stress values which occurred during the simulation for each irradiation condition. The comparison of the results given by our model and experimental data from previous experiments is presented in **Fig. 8**.

Because damaged zones are slightly oval, we averaged the diameter of the long and short axes of the ellipse. Static irradiation diameters are averaged over the 6 repetition experiments and error bars are scattering information (standard deviation) from the 6 experiments. We considered the microscope measurement uncertainty negligible compared to the scattering of the damaged zone diameters. Scattering information is not available for the dynamic mode because the experiment was not repeated. Additionally, the sensitivity of the simulation results to laser beam power variations is presented on the graph. Along with the thermal conductivity, it was estimated to be the parameter with the greatest impact on r_r. The ±5 W criterion comes from results obtained in **section 4.1**.

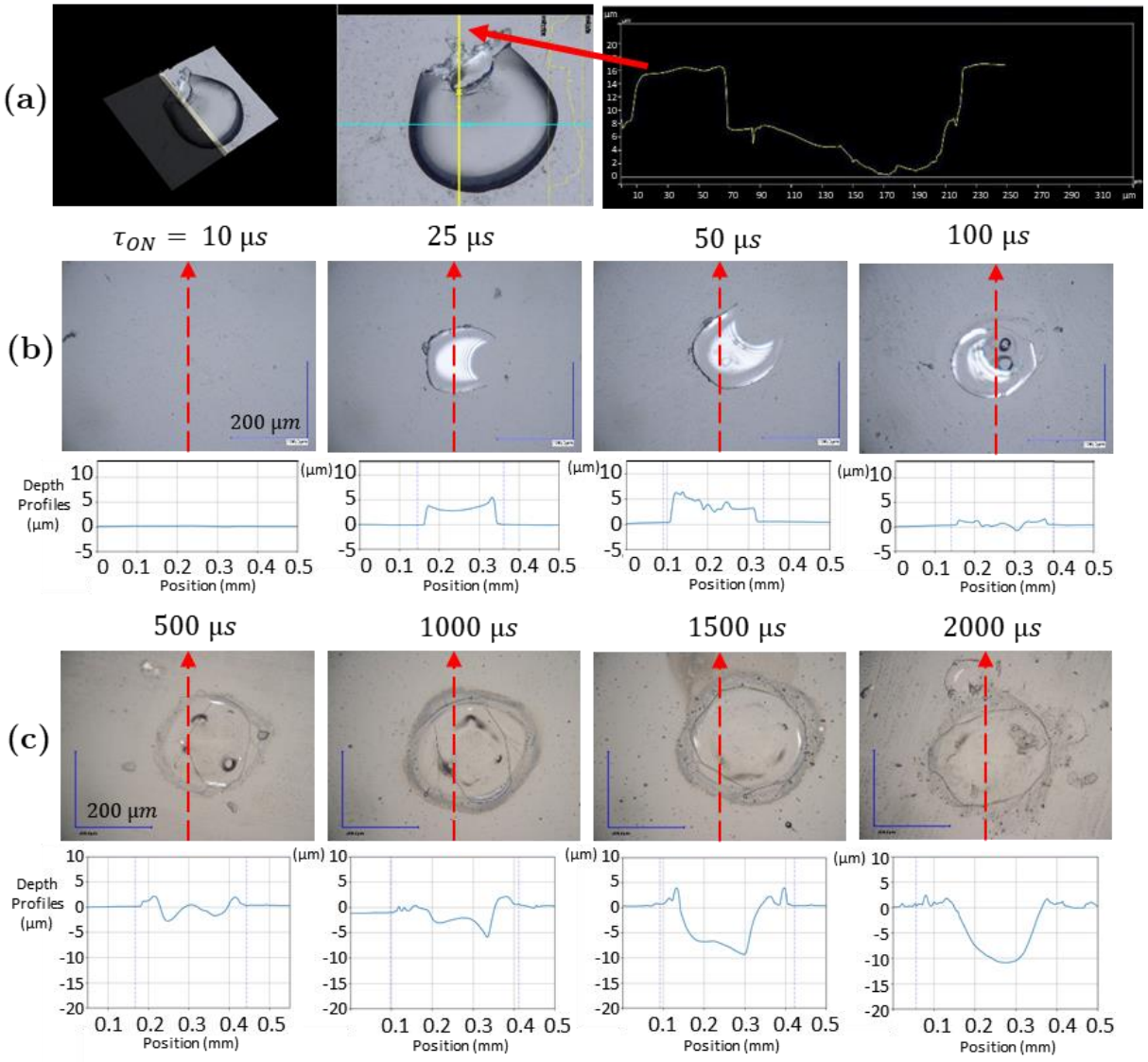

Fig. 5 Static irradiation damaged zones on SDL glass for increasing τ_{ON} . Each picture scale and profile X-axis is displayed with the same scale factor (200 µm). Each profile Y-axis is displayed with the same scale factor. Red arrows correspond to the profile measurement path. **(a)** The glass fragment has been removed by air blowing. This allowed 3D surface profile measurements with the KEYENCE. The profile on the right corresponds to the yellow arrow of the figure in the middle. **(b)** Microscope photograph and corresponding stylus profilometry. **(c)** Microscope photograph of damaged sites and corresponding stylus profilometry.

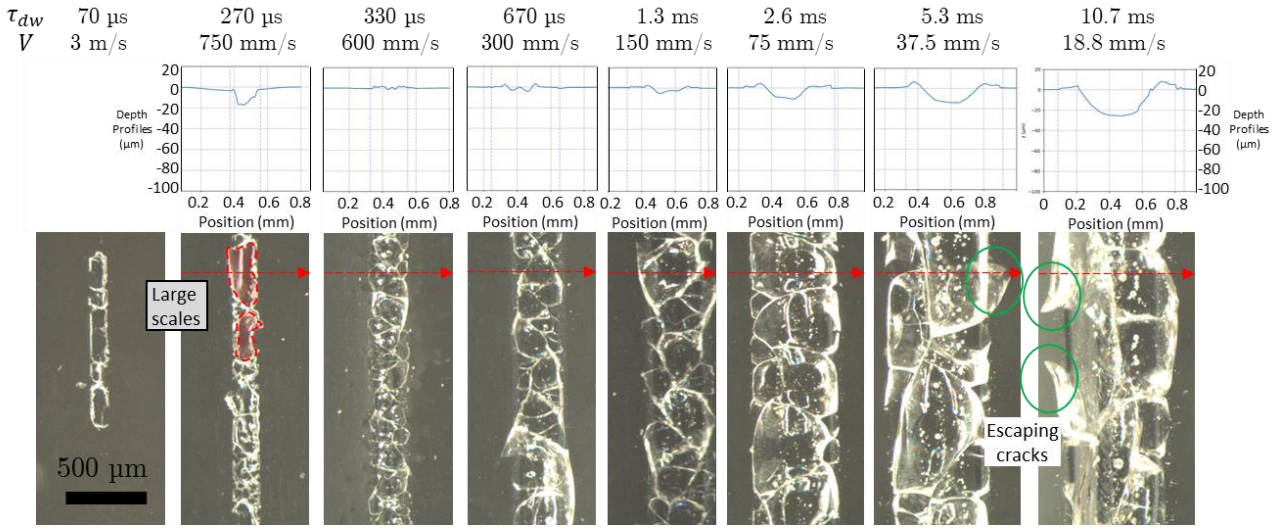

Fig. 6 Dynamic mode microscope photograph and corresponding transverse surface profile (red dashed arrows). Dwell-time τ_{dw} is mentioned above each photograph. V is the equivalent velocity. The horizontal axes of the charts and the pictures are represented with the same scale factor. (dashed contours) highlight large glass scales. (green circles) are escaping cracks.

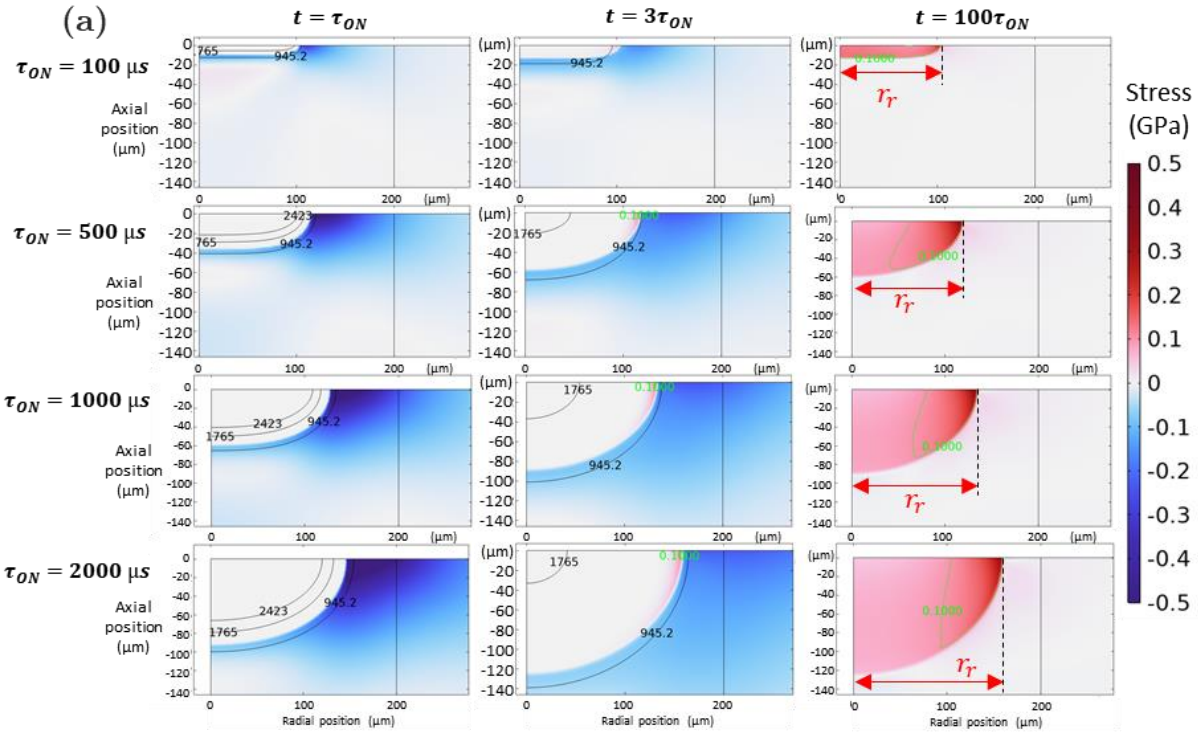

(b)

τ_{ON} (µs)	10	25	50	100	500	1000	2000	3000
Tensile (GPa)	0	0.2	0.24	0.28	0.41	0.41	0.36	0.34
Compressive (GPa)	-0.13	-0.21	-0.23	-0.35	-0.72	-0.86	-0.95	-0.96

Fig. 7 (a) Images of the RZ-plane showing numerical results of CO_2 laser heating of SDL glass. The color map shows the radial component of the viscoelastic stress tensor in GPa (blue is compressive and red is tensile). (black lines) are temperature isovalues labelled with the corresponding temperature in K. (green lines) are stress isovalues labelled with the corresponding stress in GPa. r_r is the measured radius of the relaxed zone at RT. **(b)** Simulation extremum stress for each value of τ_{ON}.

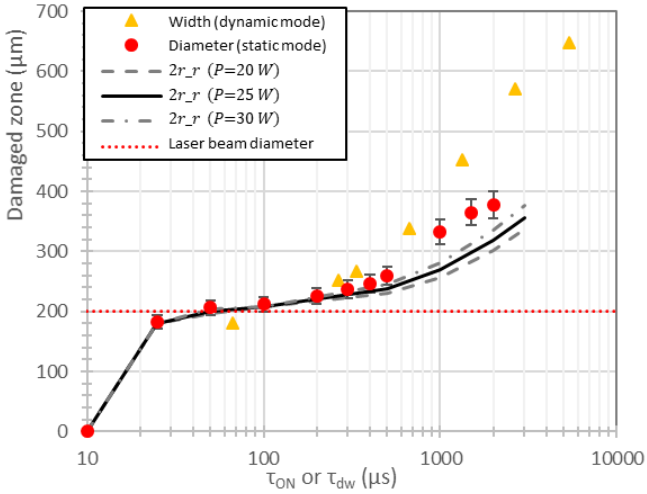

Fig. 8 Comparison between damaged zone width for dynamic mode (experimental), damaged zone diameter for static mode (experimental) and relaxed zone diameter $2r_r$ (simulation) versus exposure time. Laser power influence on $2r_r$ and laser beam diameter are also plotted.

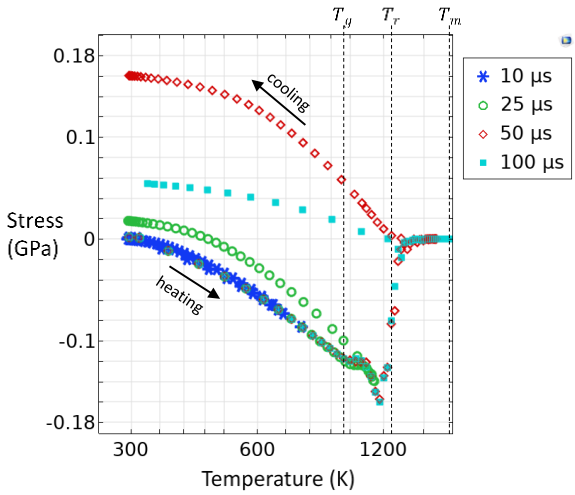

Fig. 9 Radial component of the transient stress σ_{rr} versus temperature at the surface center point. (r=0, z=0) Vertical lines correspond respectively from left to right to the glass transition temperature, stress relaxation point (1250 K) and melting temperature. All traces correspond to different values of τ_{ON}. Positive stress is tensile and negative is compressive.

4.4 Transient thermal stress

From the simulation model that we implemented, we plotted on **Fig. 9** the radial component of the stress σ_{rr} versus the temperature for the heating and the cooling cycles at the surface center point (r=0, z=0). This measure allows us to gain greater insight into the transient stress experienced by the glass during thermal cycles and to estimate the relaxation temperature of our sample. Glass transition temperature and melting temperature are also plotted to show that the relaxation process occurs in between those values.

This result illustrates the transient stress relaxation process, as reported by Bennett *et al.* [17]. All the curves start from RT and stress is equal to zero. Then, the temperature rises, and stress rapidly increases toward negative values (compressive stress) and, at some point, the stress drops to 0 GPa in less than 10 µs independently of the irradiation condition. The temperature reaches its maximum and then slowly decreases until some strain freezing temperature is reached. Note that if the relaxation temperature is not reached (10 µs) the material evolves under elastic deformation and no tensile stress is created.

5. Discussion

5.1 Partial texturing regime

The partial texturing regime is identified by an engraving rate less than 100% and greater than 0% which corresponds, for the static mode, to 25 µs≤τ_{ON}≤500 µs (**Fig. 5**) and for the dynamic mode to τ_{dw}≤270 µs (**Fig. 6**).

The accuracy of our model in this regime for the static mode is evidenced by the fact that the smallest non-zero cracking rate value lies, for both experimental and simulated results, between τ_{ON}= 10 µs and 25 µs (**Fig. 8**).

Moreover, in this regime, the relaxed zone radius (simulation) and the damaged zone radius (experimental) remain equivalent to the laser beam radius. This comes from the fact that the heat is mainly directed toward the Z-axis and, thus the temperature remains almost constant along the R-axis.

Additionally, the fracture morphologies, see **Fig. 5** in this regime, do not exhibit any forking effect [31], which means that the stress intensity is relatively low compared to the full texturing regime. Because this stress is relatively low, the crack propagates along the most stressed zone which describes a circle around the relaxed zone. During crack propagation, when enough stress is released, the crack stops before completing the full round of the fragment, leaving it partially attached to the bulk. The rise of the surface in this regime is explained by the compressive stress present in the relaxed area along the Z component of the viscoelastic stress tensor. Such fragments can be removed during or after the irradiation process and leave large mirror-like surfaces, named glass scale-shaped fragments that appear transparent to the naked eye, see **Fig. 6** and **Fig. 5 (a)**. Because they appear transparent, we need to avoid this phenomenon for our application. Lastly, it has to be noted that the scale-shaped glass fragments (**Fig. 5 (a)**) typically found in this range seem to have random in-plane directions. The random distribution of orientations means that there is no preferential direction of propagation for the crack, and thus no significant residual forces in the glass before and during the process.

5.2 Full texturing regime

The full texturing regime is identified for moderate exposure which corresponds for a static source to 500 µs≤τ_{ON}≤1000 µs (**Fig. 5**), and for a moving source to 330 µs≤ τ_{dw}≤1.3 ms (**Fig. 6**). This regime is delimited by a reliable engraving condition (engraving rate = 100%) as the lower τ_{ON} bound, and no significant material removal as the upper τ_{ON} bound.

As more energy is delivered to the sample than in the partial texturing regime, the temperature can rise until the vaporization point of silica is reached. In this case, the glass is totally molten and boiling can occur. Bubbles form in the melt and travel toward the surface. Following All-

cock et al. [11] and glass manufacturers [32], the nature of these bubbles is likely to be dioxygen and sodium evaporating from the SDL glass melt. When the gaseous components reach the surface, they may be excited by the laser radiation and form the typical yellowish plasma plume above the irradiated area (no images provided). When bubbles reach the surface and burst, the glass melt surface is deformed. If, during the cooling phase, the temperature falls below the strain freezing temperature T_r (**Fig. 9**) while bubbles are reaching the surface, the deformed melt surface will freeze, leaving blowholes that appear darker in **Fig. 5** and **Fig. 6**.

Moreover, the glass surface is fractured into smaller fragments and more forking effects are visible than in the previous regime. This qualitatively indicates a greater stress level which is confirmed by the simulation on **Fig. 7 (b)** where the tensile stress level is the greatest for 500 µs≤τ_{ON}≤1000 µs. The higher number of fractures and the presence of trapped bubbles are very interesting for our application as they scatter incoming light, making the engraving more visible. However, the damaged zone has to be as small as possible to ensure high resolution marking.

5.3 Material removal regime

The last regime is called the material removal regime (long exposure). It is identified by a surface profile presenting a crater or groove deeper than 5 µm. This regime is reached in static mode for τ_{ON}>1000 µs (**Fig. 5**) and in dynamic mode for τ_{dw}>1.3 ms (**Fig. 6**).

In this regime, the heated glass reaches its vaporization point (≈3700 K) [33]. The evaporation process induces a recoil pressure on the melt bath that is ejected by the latter, forming a crater. The proportion of evaporated matter over pressure-ejected matter is difficult to quantify without *in situ* recording. However, we can qualitatively estimate that the pressure-ejecting process is not the dominant mechanism as the crater walls' volume and the quantity of glass redeposited in the surrounding area seem small compared to the amount of matter missing in the crater. For example, in **Fig. 5** at τ_{ON}=1500 µs, the wall volume projected by the revolution of the stylus profile around its center point does not seem to compensate for the matter missing inside the crater.

Moreover, we can see from **Fig. 7 (b)** that the critical compressive stress of glass (0.8 GPa) is reached in this regime. Despite the short duration of this crack initiation state, which lasts for a duration equivalent to the respective τ_{ON}, compressive cracking may occur. However, it should be remembered that, similarly to the behavior of the engraving rate presented in **Fig. 4**, the engraving rate in this state will not be 100% in the near threshold range. Moreover, the melt pool continues to increase until approximately $t=3\tau_{ON}$ which will melt the hypothetical compressively cracked zone. For much higher exposure time, *e. g.* τ_{dw}>5 ms (**Fig. 6**), cracks propagate outside the irradiated zone (escaping cracks). These cracks may be compressive-stress induced cracks that can lead to destruction of the sample.

Additionally, the simulation results in this range underestimate the relaxed zone radius by 14%. This deviation from the experimental results can be explained by the fact that we did not consider material ejection in the simulation. The radius of the simulated relaxed zone would have been larger if material ejection had been considered. Moreover, the properties simulator seems to have overestimated the T_g, T_m and VFT coefficients, thereby reducing the relaxed zone radius. These properties are very critical because they are the parameters responsible for the relaxation process which is the key phenomenon for explaining glass cracking during the cooling phase.

Lastly, the use of the dwell time criterion for comparison between static and moving source shows a satisfactory trend but the experimental results rapidly diverge from the static mode diameters in this regime. A deeper characterization of the laser beam profile could enhance the precision of this comparison criterion and a 3D model will help us to understand the stress field differences between static and dynamic mode.

6. Conclusion

The primary objective of this article was to study the cracking mechanisms of SDL glass bottles irradiated by an industrial CO_2 laser system for the purpose of decorating through engraving. By irradiating SDL glass samples in both static and dynamic modes, we varied the exposure times while maintaining continuous power (25 W). The resulting damaged zone diameters were carefully examined using microscopy and profilometry, leading us to identify three distinct cracking regimes: partial texturing, full texturing, and material removal. Each regime was observed to occur with increasing exposure time and exhibited unique characteristics, which we thoroughly analyzed to understand their underlying mechanisms.

To validate the mechanisms, we employed COMSOL Multiphysics to simulate the interaction between the laser and the glass material in a 2D axisymmetric plane. By comparing the threshold exposure time required for cracking, we confirmed the accuracy of our simulation model. Additionally, we conducted a comparative analysis between the simulated relaxed zone diameter and the experimental damaged zone diameter. Remarkably, we found a strong correlation in the partial texturing and full texturing regimes, with the simulation predicting the damaged zone radius with a relative uncertainty of ±3%. However, the accuracy decreased to +14% in the material removal regime, as the simulation did not account for the groove depth of up to 20 µm observed in experimental results. This discrepancy may be attributed to the relatively high values of viscosity-to-temperature relation (VFT coefficients) and T_g given by the material properties simulator, which deviate from typical SDL glass values. Thus, incorporating temperature-to-viscosity measurements specific to our samples would enhance the precision of our model.

Furthermore, we employed a physical criterion τ_{dw} to compare the static and dynamic modes, finding a satisfactory trend. However, the damaged zone diameter in the dynamic mode exceeded and deviated from that in the static mode. To gain deeper insights into crack initiation and propagation in the dynamic mode, it is imperative to conduct further investigations concerning the beam intensity profile and perform 3D simulations. Finally, our future research aims to expand the knowledge surrounding SDL glass cracking initiation and the propagation process, particularly for large-scale surface texturing applications.

Acknowledgments

The authors are grateful for the financial support from the ANRT (Agreement number: 2012-0278) and to the Région Centre-Val de Loire in the framework of the ARD MATEX-SAILOR project. We would like to extend our sincere gratitude to S. Desprez (DWS) for providing the glass samples and to A. Ricci (DWS) for lending us the CO_2 laser.

References

[1] S. Chandra, S. Verma, W. M. Lim, S. Kumar, and N. Donthu: Psychol. Mark., 39, (2022) 1529.
[2] M. Pizzetti and M. Gibbert: J. Consum. Mark., 35, (2018) 512.
[3] M. R. B. Andreeta, L. S. Cunha, L. F. Vales, L. C. Caraschi, and R. G. Jasinevicius: J. Micromech. Microeng., 21, (2011) 025004.
[4] B. Gu: Proc. SPIE, Vol. 6106, (2006) 610601.
[5] A. N. Samant and N. B. Dahotre: Journal of the European Ceramic Society, 29, (2009) 969.
[6] M. Testa, O. Malandrino, M. R. Sessa, S. Supino, and D. Sica: Sustainability, 9, (2017) 1752.
[7] G. L. Robertson: "Food packaging: principles and practice" ed. by CRC press, (2013) 231.
[8] M. K. Gunde: Phys. B: Condens., 292, (2000) 286.
[9] R. Kitamura, L. Pilon, and M. Jonasz: Appl. Opt., 46, (2007) 8118.
[10] J. Martin: "Materials for engineering" ed. by Woodhead Publishing, (2006) p. 134.
[11] G. Allcock, P. E. Dyer, and G. Elliner, and H. V. Snelling: J. Appl. Phys., 78, (1995) 7295.
[12] A. Rolo, J. Coelho, and M. Pires: Proc. ICALEO, Vol. 28 (2005) 506.
[13] B.-J. Meyer, G. Staupendahl, F. A. Müller, and S. Gräf: J. Laser Appl., 28, (2016) 012002.
[14] P. Deprez, C.-F. Melian, F. Breaban, and J.-F. Coutouly: J. Mater. Sci. Technol., 2, (2012) 32.
[15] K. Yamamoto, N. Hasaka, H. Morita, and E. Ohmura: J. Laser Appl., 20, (2008) 193
[16] G. Savriama, F. Baillet, L. Barreau, C. Boulmer-Leborgne, and N. Semmar: J. Laser Appl., 27, (2015) 032009.
[17] T. D. Bennett, L. Li: J. Appl. Phys., 89, (2001) 942
[18] T.-R. Shiu, C. P. Grigoropoulos, D. G. Cahill, and R. Greif: J. Appl. Phys., 86, (1999) 1311.
[19] A. Fluegel: Statistical Calculation and Development of Glass Properties (2007) https://glassproperties.com/
[20] J. E. Shelby, M. Lopes: "Introduction to Glass Science and Technology" ed. by Royal Society of Chemistry, (2007) 250.
[21] D. Bäuerle: "Laser Processing and Chemistry" ed. by Springer Berlin Heidelberg (2011) 131.
[22] N. P. Bansal, R. H. Doremus: "Handbook of Glass Properties" ed. by San Diego: Academic Press, (1986) 372.
[23] C. Guillemet, R. Gy, M. Labrot, D. Neuville, A. Sipp, and P. Richet: Proc. XVI International Congress on Glass., Vol. 2, (1992) 183.
[24] M. A. Meyers and K. K. Chawla: "Mechanical Behavior of Materials", ed. by Cambridge University Press, (2009) 688.
[25] M. Rubin: Sol. Energy Mater., 12, (1985), 275
[26] M. J. Meyland, J. H. Nielsen, and C. Kocer: J. Build. Eng., 44, (2021) 102966.
[27] S. Tan, X. Yao, S. Long, X. Zhang, and S. Zang,: J. Non-Cryst., 516, (2019) 14.
[28] M. M. Junda and N. J. Podraza: Surf. Sci. Spectra, 25, (2018) 016001.
[29] L. Duffrene, R. Gy, J. E. Masnik, J. Kieffer, and J. D. Bass: J. Am. Ceram., 81, (1998) 1278.
[30] J. M. Liu: Opt. Lett., 7, (1982) 196
[31] M. D. Hayes, D. B. Edwards, and A. R. Shah: "Fractography in Failure Analysis of Polymers" ed. by Elsevier, (2015) 48.
[32] H. Van Limpt, H. Beerkens, and O. Verheijen: J. Am. Ceram., 89, (2006) 3446.
[33] S. M. Karazi, I. U. Ahad, and K. Y. Benyounis: "Reference Module in Materials Science and Materials Engineering", ed. by Elsevier, (2017) 11

(Received: April 19, 2023, Accepted: July 25, 2023)